Materials Today: Proceedings xxx (xxxx) xxx

Contents lists available at ScienceDirect

Materials Today: Proceedings

journal homepage: www.elsevier.com/locate/matpr

Microstructure, magnetic properties of Ho^{3+} substituted Ni-Cu-Zn spinel ferrites and application for one pot synthesis of dihydropyrimidinones

U.M. Mandle [a], R.M. Tigote [b], K.S. Lohar [c], B.L. Shinde [d,*]

[a] Department of Chemistry, Sangameshwar College, Solapur 413001, M.S., India
[b] Department of Chemistry, Osmanabad Sub-Centre, Dr. Babasaheb Ambedkar Marathwada University, Aurangabad 413501, M.S., India
[c] Department of Chemistry, Shrikrishna Mahavidyalaya, Gunjoti, 413606 Osmanabad, M.S., India
[d] Department of Chemistry, Waghire College, Saswad, Pune 412301, M.S., India

ARTICLE INFO

Article history:
Available online xxxx

Keywords:
Sol-gel auto combustion
Ni-Cu-Zn ferrites
Saturation magnetization
Dihydropyrimidinones

ABSTRACT

Nanoparticles of Ni-Cu-Zn spinel ferrites with Ho^{3+} substitution were synthesized through the sol–gel auto combustion route. It is illustrated from thermogravimetric analysis and differential thermal analysis curve that the decomposition of precursors takes place in the temperature range 350–460 °C. The Energy dispersive spectroscopy confirmed the mixing of the Fe, Ni, Cu, Zn, Ho and oxygen elements in stoichiometry proportion in pure and substituted spinel ferrites with desired stoichiometry. X-ray diffraction pattern confirmed the formation of cubic spinel structure without any impurity phases. Lattice constant, X-ray density increases while average crystallite size decreases with increased Ho^{3+}substitution in Ni-Cu-Zn ferrites. The two strong IR absorption bands observed in the range 565–568 (ν_1) and 409–438 (υ_2) cm^{-1}. The obtained crystallite size lies between of 18 – 26 nm, confirmed from transmission electron microscopy. The microstructures of the calcinated spinel ferrites were evaluated by SEM and TEM. It is observed that the increase in concentration of Ho^{3+} ions saturation magnetization decreases. Prepared Ho^{3+} substituted Ni-Cu-Zn spinel ferrites were used as catalyst to synthesize the 3,4-dihydropyrimidin-2(1H)-ones.[copyright information to be updated in production process]

Selection and peer-review under responsibility of the scientific committee of the International Web Conference on Advanced Materials Science and Engineering.

1. Introduction

Nanoscience and Nanotechnology is the technology associated with materials in nanometer range and appliances based on them [1]. Ferrites are chemical composites with iron (III) oxide Fe_2O_3 as their major constitutes [2]. The electrical conduction and magnetic interactions of the ferrites are significantly altered by substitution of trivalent or tetravalent cations and also affected by the site occupancy of cations between the tetrahedral A and octahedral B sites of spinel structure [3]. By tailoring the stoichiometry of the ferrite system structural, electrical and magnetic properties can be tuned [4]. The spinel ferrites have versatile applications such as magnetic drug delivery [5], information storage [6], super capacitor [7], magnetic refrigeration [8], gas sensors [9], and catalyst [10] etc.

Ni-Cu-Zn ferrites have more attention of researchers due to their outstanding characteristics such as low magnetic losses, high permeability and high resistivity, which are suitable for microwave applications [11]. The doping of trivalent rare-earth cations in ferrites are becoming the important components for sophisticated applications [12]. The substitution of little quantity of rare-earth cations improves structural, electrical and magnetic properties of ferrites [13].

One-pot multicomponent reactions have more advantages over traditional reactions due to their rapidity, simplicity, atom-economy and shorter synthetic route [14] for the synthesis of bio-active molecules [15]. Now days, the use of heterogeneous catalysts has established significant interest in various disciplines, i.e. organic synthesis, using heterogeneous catalysts have great advantage of catalyst recycle as compared to homogeneous catalyst. Iron oxide nanoparticles are used as heterogeneous catalyst as it is separated without filtration simply applying external magnetic field [16]. The catalytic activity of spinel ferrites for these reactions arises due to the ease iron can switch its oxidation state between 2+ and 3+ and hence spinel structure ferrites have stability under extremely reducing conditions. The Fe^{3+} reduced to Fe^{2+} without

* Corresponding author. Email address: shindebl1981@gmail.com (B.L. Shinde)
E-mail address: shindebl1981@gmail.com (B.L. Shinde).

https://doi.org/10.1016/j.matpr.2021.04.027
2214-7853/
Selection and peer-review under responsibility of the scientific committee of the International Web Conference on Advanced Materials Science and Engineering.

varying lattice arrangements; therefore original sate is obtained on reoxidation [17].

Now days, magnetic spinel ferrites used as efficient catalyst in different chemical transformations such as synthesis of diazepine derivatives [18], α-amino nitriles [19], 1,1-diacetates from aldehydes [20], etc. Dihydropyrimidinones have synthesized by Pietro Biginelli in 1893, by a one-pot three-component condensation of benzaldehyde, ethyl acetoacetate and urea under robustly acidic environment [21]. Also Dihydropyrimidinones synthesized by microwave irradiation [22], ionic liquids [23] and using different types of catalysts such as lanthanide triflate [24], $Sr(OTf)_2$ [25], nano magnetic-supported sulfonic acid [26], Fe(III) tosylate [27], $FeCl_3$-supported nanopore silica [28], etc.

The present report deals with the modification in the structural and magnetic properties of Ho^{3+}substituted Ni-Cu-Zn spinel ferrites with composition $Ni_{0.2}Cu_{0.2}Zn_{0.6}Fe_{2-x}Ho_xO_4$ (x = 0.00, 0.02, 0.04, 0.06 and 0.08). The targeted samples were synthesized by sol–gel auto-combustion method. The prepared samples at nano scale regime were used as a catalyst for one pot three component synthesis of Dihydropyrimidinones.

2. Materials and methods

2.1. Preparation of $Ni_{0.2}Cu_{0.2}Zn_{0.6}Fe_{2-x}Ho_xO_4$ ferrites:

The nano-crystalline powders of $Ni_{0.2}Cu_{0.2}Zn_{0.6}Fe_{2-x}Ho_xO_4$ (x = 0.00, 0.02, 0.04, 0.06, and 0.08) prepared using sol–gel auto-combustion method [4]. The stoichiometric quantities of analytical grade reagents of corresponding metal nitrates were dissolved in deionized water. The aqueous citric acid solution added in the metal nitrates to citric acid ratio of 1:3 and then NH_3 solution added to adjust pH ≈ 7 of solution. The resulting solution was heated on hot plate (90 °C) with continuous stirring. After some time the solution turns viscous and converted in to brown gel, with complete removal water molecule gel starts frothing and later on automatically get burnt. The process of auto-combustion accomplished in a minute, resulting in the formation of the brown ashes known as precursors. Calcination temperature is confirmed from TGA/DTA curve and all the precursors calcinated at 460 °C for four hours, gives final spinel ferrites.

Thermal analysis carried using simultaneous TGA and DTA of precursors at heating rate 10°C/min in the range 25 °C to 800 °C on SDT Q600 V20.9 Build 20 in air. With EDAX, Inca Oxford attached to the SEM the composition of calcinated samples determined. The structural parameters investigated by X-ray diffraction Phillips-3710 X-ray diffractometer employed with Cu-K_α radiation (λ = 1.5405 Å) were used in the present study. Microstructure investigated by JEOL-JSM-5600-N Scanning Electron Microscope and on Philips-CM-200 Transmission Electron Microscope. Magnetic measurements carried at room temperature using PARC EG&G vibrating sample magnetometer.

2.2. Preparation of 3,4-dihydropyrimidin-2(1H)-ones:

Aldehyde (**1**) (10 mmole), 1,3-dicarbonyl compound (**2**) (10 mmole), urea (**3**) (15 mmole) were dissolved in ethanol to which catalyst $Ni_{0.2}Cu_{0.2}Zn_{0.6}Fe_{2-x}Ho_xO_4$ (20 mol %) spinel ferrite was mixed and then reaction mixture was heated at 80 °C with constant stirring for suitable time (monitored by TLC). After completion of reaction, catalyst was separated by keeping the catalyst at the bottom of flask magnetically by using a strong permanent magnet, and the solution was removed. The entire mixture was then transferred into ice water, the precipitate of product obtained which is separated by filter paper, washed by water and dried. The product was purified by recrystallization using ethanol as a solvent. All the synthesized compounds were characterized by ^1H NMR, Mass (ES-MS) and melting point.

3. Results and discussion

3.1. Thermal analysis

Fig. 1a-e represents TGA/DTA curves of $Ni_{0.2}Cu_{0.2}Zn_{0.6}Fe_{2-x}Ho_xO_4$ (x = 0.0 to 0.08). All TGA curves shows two weight loss steps associated with endothermic and exothermic DTA peaks. The first weight loss step in the temperature 30–100 °C range is corresponding to endothermic peak around 80 °C, is due to evaporation of residual water from precursor. The second weight loss step in the 350–460 °C temperature region was corresponding to the exothermic peak around 400 °C, due to the decomposition of unreacted citric acid. No weight loss observed above 460 °C, representing the presence of only $Ni_{0.2}Cu_{0.2}Zn_{0.6}Fe_{2-x}Ho_xO_4$ in this temperature range. Therefore, the prepared precursors calcinated at 460 °C for four hour to get $Ni_{0.2}Cu_{0.2}Zn_{0.6}Fe_{2-x}Ho_xO_4$ spinel ferrites.

3.2. Elemental analysis

The chemical compositions of $Ni_{0.2}Cu_{0.2}Zn_{0.6}Fe_{2-x}Ho_xO_4$ ferrite nanoparticles are determined by EDAX. Fig. 2(a) and (b) shows the EDAX patterns for the $Ni_{0.2}Cu_{0.2}Zn_{0.6}Fe_{2-x}Ho_xO_4$, ferrite nanoparticles (x = 0.00 to x = 0.08). The EDAX patterns confirmed the homogeneous mixing of the elements in desired composition. The values of observed and theoretical percentage of Fe, Ni, Cu, Zn, Ho and oxygen are in good agreement with theoretical % values of element (Table 1).

3.3. Structural analysis

Fig. 3 shows the XRD patterns of the calcinated $Ni_{0.2}Cu_{0.2}Zn_{0.6}Fe_{2-x}Ho_xO_4$ ferrites. XRD patterns illustrates single phase cubic spinel ferrite (JCPDS # 00–52-0277 and 00–74-0444) [29] was obtained for the pure Ni-Cu-Zn ferrite and no other visible peak corresponding to the second phase was observed, which illustrated that Ho^{3+} could be entirely solid-soluted in cubic spinel structure or that the amount of the other phase was too small to be identified by XRD [30].

The lattice constant 'a' determined by equation discussed elsewhere [30] and given in Table 2. The calculated lattice constants are within range of 8.417 Å to 8.429 Å, increases with in Ho^{3+} ion concentration. The variation in 'a' was mainly attributed to difference between the ionic radii of constituent ions. Here, smaller Fe^{3+} (0.67 Å) ions are substituted by larger Ho^{3+} (1.04 Å) ions.

X-ray density 'd_x' of Ho^{3+} substituted Ni-Cu-Zn ferrites samples were calculated using the following formula and tabulated in Table 2,

$$dx = \frac{8M}{Na^3} \quad (1)$$

Where 'a' is lattice constant, 'N' is the Avogadro's number and 'M' is molecular weight. The X-ray density in present spinel ferrites increased with Ho^{3+}ion concentration, due to the increased molecular weight of spinel ferrite.

Crystallite size (D_{XRD}) was obtained from the XRD pattern by employing Debye Scherrer method [31]. The calculated D_{XRD} lies within the range of 18–26 nm (Table 2). The crystallite size in present spinel ferrites was decreased with Ho^{3+} concentration. It reveals that when Ho^{3+} ion is substituted in the place of Fe^{3+} ion, it may induce a crystalline anisotropy and this crystalline anisotropy increases with Ho^{3+} concentration. Apart from this with increasing Ho^{3+} concentration, volume strain inside the material

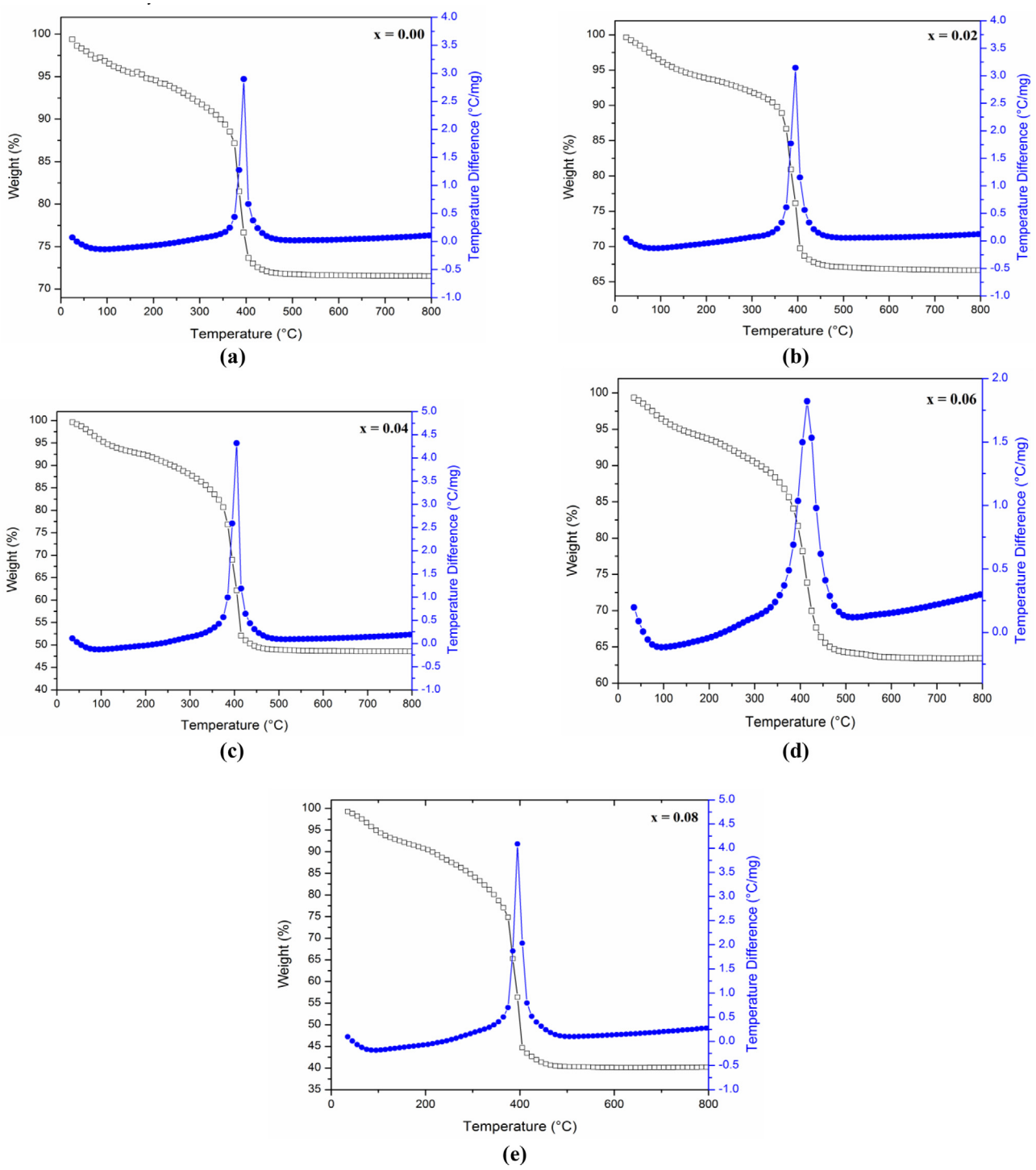

Fig. 1. a-e Typical TGA-DTA plots for precursors of $Ni_{0.2}Cu_{0.2}Zn_{0.6}Fe_{2-x}Ho_xO_4$ (x = 0.00 to 0.08).

will also increase. Therefore, for a system to remain in stable equilibrium, crystal anisotropy and volume strain should balance each other. In order to relax the volume strain, the crystallite size decreases with the increase of Ho^{3+} ions [32].

The percentage porosity 'P' of all the samples was calculated using the values of X-ray density and bulk density [33]:

$$P = 1 - \frac{d_B}{d_x} \times 100\% \quad (2)$$

Where, d_B and d_x are the bulk and X-ray densities respectively.

The porosity 'P' in present spinel ferrites is increased with Ho^{3+} substitution. The increase the grain boundaries of the fine particles may result in enhancement in 'P', that illustrate the porous structure of the $Ni_{0.2}Cu_{0.2}Zn_{0.6}Fe_{2-x}Ho_xO_4$, ferrites.

The hopping lengths L_A and L_B were calculated using following equations [4],

$$L_A = \frac{a\sqrt{3}}{4} \quad (3)$$

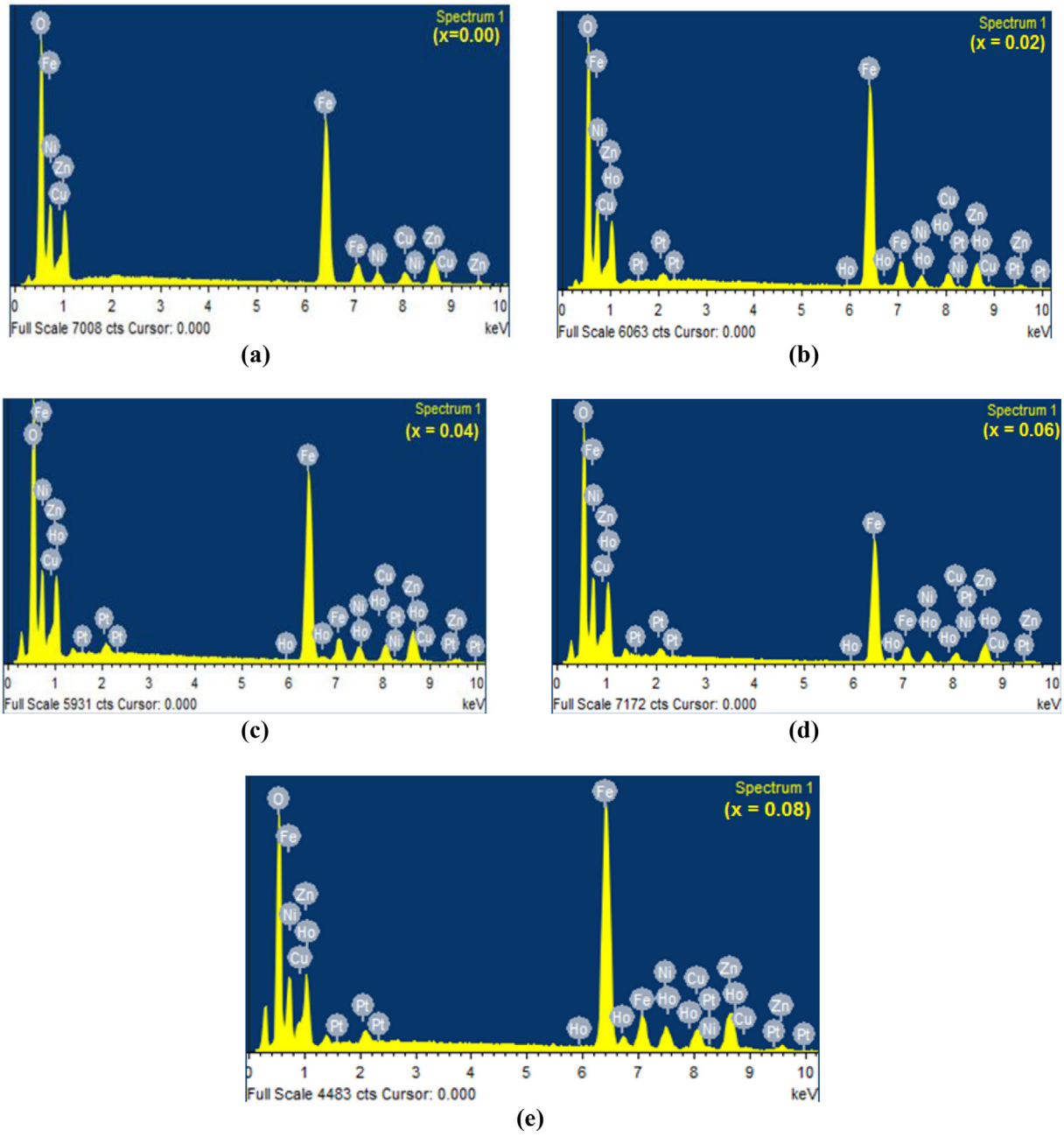

Fig. 2. a-e EDAX patterns for $Ni_{0.2}Cu_{0.2}Zn_{0.6}Fe_{2-x}Ho_xO_4$ (x = 0.00 to 0.08).

Table 1
Observed and Theoretical elemental % for $Ni_{0.2}Cu_{0.2}Zn_{0.6}Fe_{2-x}Ho_xO_4$ system.

Comp.'x'	Observed %						Theoretical %					
	Ni	Cu	Zn	Fe	Ho	O	Ni	Cu	Zn	Fe	Ho	O
0.00	4.85	5.38	16.34	46.37	0.00	27.06	4.90	5.31	16.39	46.66	0.00	26.74
0.02	4.79	5.33	16.22	45.47	1.47	26.72	4.86	5.26	16.24	45.78	1.37	26.49
0.04	4.75	5.28	16.10	44.57	2.85	26.45	4.82	5.21	16.09	44.90	2.74	26.24
0.06	4.74	5.20	15.99	43.97	4.28	25.82	4.78	5.16	15.94	44.02	4.11	25.99
0.08	4.65	5.18	15.85	43.29	5.63	25.40	4.74	5.11	15.79	43.14	5.48	25.74

$$L_B = \frac{a\sqrt{2}}{4} \quad (4)$$

It has been observed that both the hopping lengths are increased with the Ho^{3+}ion concentration (Table 2). Variations in hopping lengths are attributed to the variation in lattice constant and ionic radii of constituent ions.

Fig. 4 illustrates the IR spectra of the $Ni_{0.2}Cu_{0.2}Zn_{0.6}Fe_{2-x}Ho_xO_4$, ferrites. The two major absorption bands observed in the range 565–568 (ν_1) and 409–438 (ν_2) cm^{-1} (Table 3). The low frequency band ν_2 observed in the range 409–438 cm^{-1} is assigned octahedral site and high frequency band ν_1 observed in the range 565–568 cm^{-1} assigned tetrahedral site. These bands are characteristics

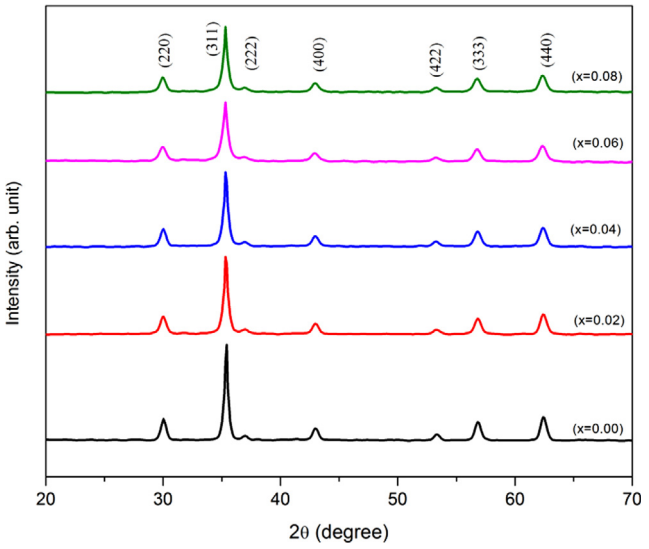

Fig. 3. XRD patterns of series $Ni_{0.2}Cu_{0.2}Zn_{0.6}Fe_{2-x}Ho_xO_4$.

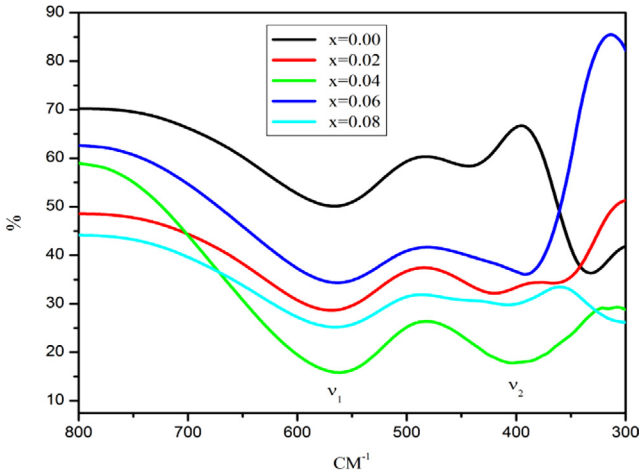

Fig. 4. IR spectra for the series $Ni_{0.2}Cu_{0.2}Zn_{0.6}Fe_{2-x}Ho_xO_4$.

features of spinel structure. The force constants of A-site (K_t) and B-site (K_o) determined by the Waldron method [34] and values given in Table 3. The values of force constants K_t and K_0 of synthesized spinel ferrites decreased from $2x10^5$ to 1.78 x 10^5 dyne/cm and 1.19 x 10^5 to 0.82 x 10^5 dyne/cm, respectively, with increase in concentration of Ho^{3+} ions. The bond lengths at A and B sites (R_A and R_B) determined using the formula given by Gorter [35]. The R_A and R_B in present spinel ferrites are increased with the substitution of Ho^{3+} ions (Table 3).

The microstructure observation of the $Ni_{0.2}Cu_{0.2}Zn_{0.6}Fe_{2-x}Ho_xO_4$ spinel has been carried out by scanning electron microscopy (SEM). Typical SEM images was presented in Fig. 5 (x = 0.02). The calcinated spinel ferrites were porous with a fine-particle microstructure. It is apparent that Ho^{3+} substituted Ni-Cu-Zn ferrites revealed a little improved dense microstructure marked with little trapped porosity.

Typical TEM images of the $Ni_{0.2}Cu_{0.2}Zn_{0.6}Fe_{2-x}Ho_xO_4$ spinel ferrite are illustrated in Fig. 6. [a) x = 0.02 and b) x = 0.08]. These TEM images indicate that sphere-like nanostructures obtained by presently employed sol–gel method. Particles are seems to uniform in particle size and microstructure and are agglomeration to some extent because of their magnetic interactions.

Selective area electron diffraction (SAED) pattern of typical composition of $Ni_{0.2}Cu_{0.2}Zn_{0.6}Fe_{2-x}Ho_xO_4$ spinel ferrite is shown in Fig. 7 (x = 0.02). The SAED patterns indicate that spinel ferrites were well distributed. The bright spot in the SAED patterns were superimposed with Debye ring confirmed the polycrystalline nature of the prepared samples. These Debye rings are assigned to lattice planes and are in good analogy with those planes obtained by the XRD data.

Particle size distributions of the respective TEM images measured by ImageJ software and typical histogram shown in Fig. 8 (x = 0.02) illustrates the average particle size distribution observed to decrease from 26.8 to 20.4 nm with increasing Ho^{3+} ion concentration.

3.4. Magnetic properties

Hysteresis loops of $Ni_{0.2}Cu_{0.2}Zn_{0.6}Fe_{2-x}Ho_xO_4$ spinel ferrite shown in Fig. 9, which illustrates that prepared samples are soft magnetic material with very low coercivity. Saturation magnetization (Ms), coercivity (Hc), and magneton number (n_B) derived from hysteresis loops and are tabulated in table 4. Coercivity obtained from the hysteresis loop was increased with the Ho^{3+} substitution. Ms for pure $Ni_{0.2}Cu_{0.2}Zn_{0.6}Fe_2O_4$ (x = 0.0) sample is 22.84 emu/g and it decreased to 16.05 emu/g for $Ni_{0.2}Cu_{0.2}Zn_{0.6}Fe_{1.92}Ho_{0.08}O_4$ (x = 0.08). The magneton number $n_{B(Obs)}$ was determined from hysteresis loops [36],

$$n_B(obs) = \frac{M_W \times Ms}{5585} \quad (4)$$

Saturation magnetization decreases while observed magneton number increased with Ho^{3+} substitution. The increase in $n_{B(Obs)}$ was attributed to the increased A-B magnetic interaction. The decrease in saturation magnetization (Fig. 9) with Ho^{3+} substitution could be explained as the surface effect becomes prominent in nanocrystalline material due to large ratio of surface to volume atoms. At the surface, structure is distorted and atoms are under the effect of strain which leads to vacancies, variety of inter atomic spacing and low coordination number. All of these factors induce a broken exchange bonds for the surface atoms, which leads to spin disorder. The disordered spins at the surface may exhibit low magnetisation [32]. The substitution of Fe^{3+} with Ho^{3+} the 'Ms' and 'Mr' may decrease as a result of decreased exchange interaction between Fe^{Td}-Fe^{Oh}, which is replaced by the weaker Fe^{Td}-Ho^{Oh}

Table 2
Lattice constant (a), X-ray density (d_x) and hopping lengths (L_A) and (L_B), crystallite size (D_{xrd}) and porosity (P).

Comp.'x'	'a' (Å)	'd_x' (g/cm^3)	L_A (Å)	L_B (Å)	P (%)	Particle size	
						D_{xrd} (nm)	TEM (nm)
0.00	8.417	5.331	3.645	2.976	27.9	26.2	26.8
0.02	8.419	5.380	3.646	2.977	28.8	23.5	23.9
0.04	8.422	5.419	3.647	2.978	30.3	22.3	22.7
0.06	8.426	5.451	3.649	2.981	31.4	21.2	21.5
0.08	8.429	5.516	3.651	2.984	31.5	19.9	20.4

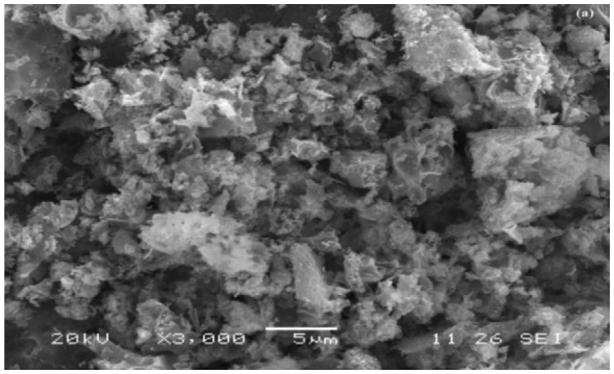

Fig. 5. Scanning electron micrograph for the series $Ni_{0.2}Cu_{0.2}Zn_{0.6}Fe_{2-x}Ho_xO_4$ (x = 0.02).

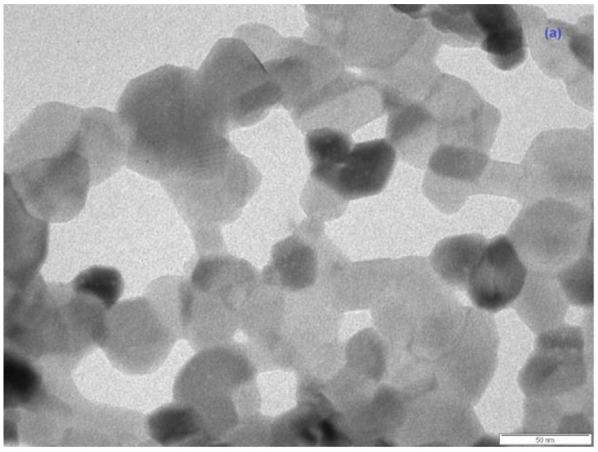

a TEM image of $Ni_{0.2}Cu_{0.2}Zn_{0.6}Fe_{2-x}Ho_xO_4$ (x=0.00)

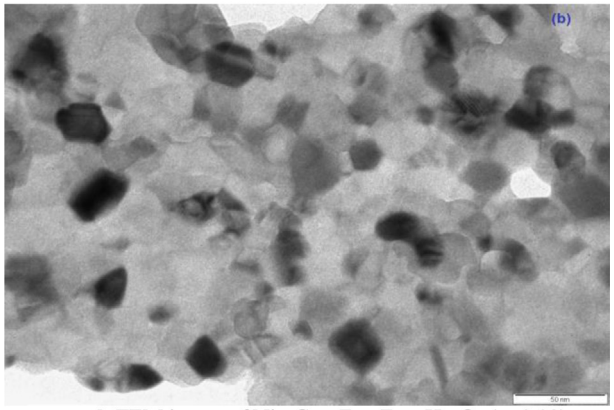

b TEM image of $Ni_{0.2}Cu_{0.2}Zn_{0.6}Fe_{2-x}Ho_xO_4$ (x=0.08)

Fig. 6. TEM images of $Ni_{0.2}Cu_{0.2}Zn_{0.6}Fe_{2-x}Ho_xO_4$;a) x = 0.00 and b) x = 0.08.

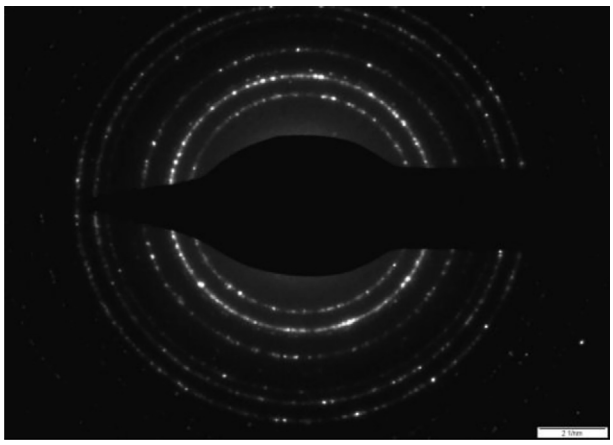

Fig. 7. SAED pattern for $Ni_{0.2}Cu_{0.2}Zn_{0.6}Fe_{2-x}Ho_xO_4$ (x = 0.00).

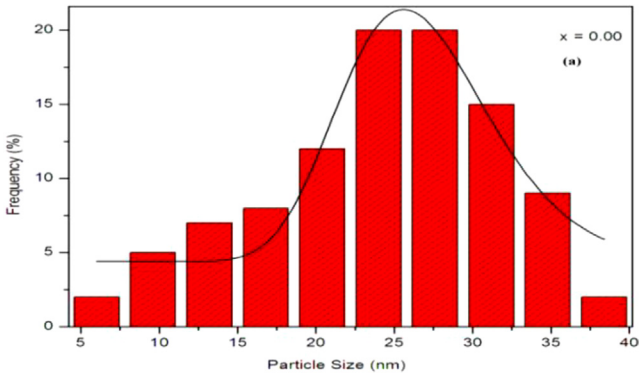

Fig. 8. Particles size distributions for $Ni_{0.2}Cu_{0.2}Zn_{0.6}Fe_{2-x}Ho_xO_4$ (x = 0.00).

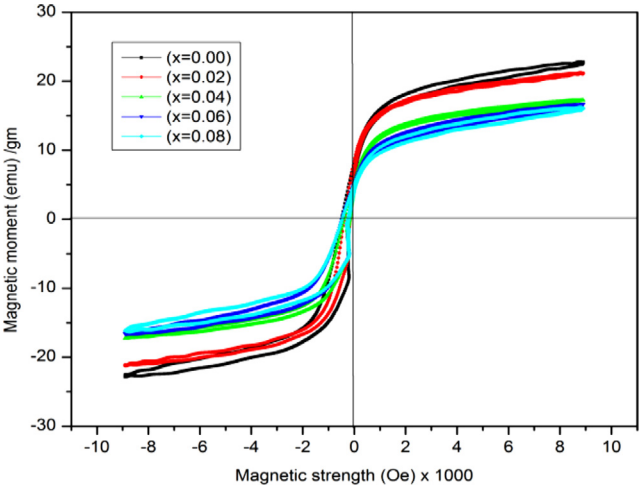

Fig. 9. Hysteresis loops of series $Ni_{0.2}Cu_{0.2}Zn_{0.6}Fe_{2-x}Ho_xO_4$.

Table 3
Band position (v_1 and v_2), Force constant (K_0 and K_t), Bond length (R_A and R_B).

Comp.'x'	Band positions		Force constants		Bond lengths	
v_1 (cm^{-1})	v_2 (cm^{-1})	K_0 x 10^5 (dyne / cm)	K_t x 10^5 (dyne / cm)	R_A (Å)	R_B (Å)	
0.00	568.0	438.2	1.19*	2.00	3.864	3.065
0.02	574.6	424.7	1.12	1.90	3.865	3.065
0.04	565.7	397.9	0.98	1.68	3.866	3.066
0.06	569.5	373.7	0.87	1.51	3.867	3.066
0.08	565.7	409.0	0.82	1.78	3.869	3.067

Table 4
Saturation magnetization(M_s), Remanant magnetization (Mr), Coercivity Hc (Oe) and magnetic moment (n_B).

Comp'x'	Mr (emu/g)	Ms (emu/g)	Hc (Oe)	$n_{B(Obs)}$ (μ_B)
0.00	10	22.84	290.08	1.978
0.02	9.5	21.28	356.80	1.846
0.04	7.7	17.23	358.24	1.517
0.06	6.6	16.5	360.64	1.481
0.08	6.7	16.05	393.04	1.459

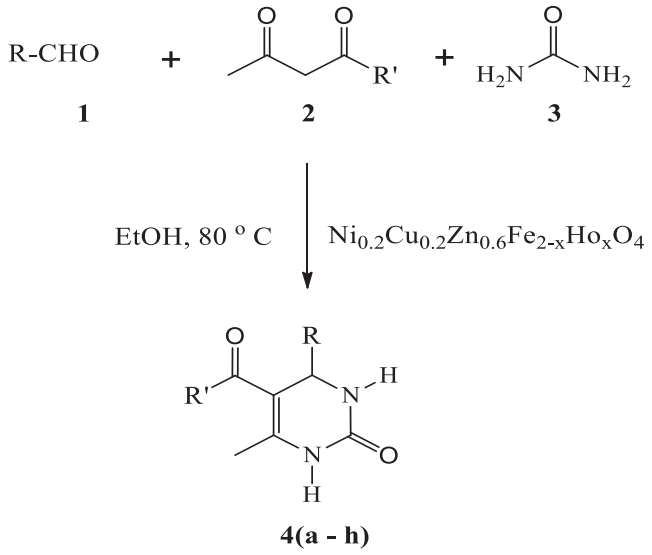

Scheme 1. Synthesis of 3,4-dihydropyrimidin-2(1H)-ones using aromatic aldehydes (1), 1,3,dicarbonyl compounds (2) and urea using 10 mol % $Ni_{0.2}Cu_{0.2}Zn_{0.6}Fe_{2-x}Ho_xO_4$ (x = 0.06) nanoparticles as catalyst.

interaction [36]. Magneton number (observed) decreases with Ho^{3+} substitution. Coercivity obtained from the hysteresis loop is observed to increase Ho^{3+}concentration (Table 4)

The net magnetic moment (n_BCal.) is determined using equation, n_BCal. = M_B-M_A; where, M_A and M_B are the A and B sublattice magnetic moments, respectively, in μ_B [37]. Values of n_BCal. for $Ni_{0.2}Cu_{0.2}Zn_{0.6}Fe_{2-x}Ho_xO_4$ were determined through cation distribution data and magnetic moment of Fe^{3+} (5μ_B), Ni^{2+} (2μ_B), Zn^{2+} (0μ_B), Cu^{3+} (1μ_B) and Ho^{3+} (10μ_B). The calculated Magneton number decreases with Ho^{3+} substitution. The magneton number (calculated) also decreases with Ho^{3+} substitution.

3.5. Application for one pot synthesis of Dihydropyrimidinones

3,4-dihydropyrimidin-2(1H)-ones was prepared by one-pot three-component condensation of aromatic aldehydes (1), 1,3,dicarbonyl compounds (2) and urea (3) using 10 mol % Ho^{3+} doped $Ni_{0.2}Cu_{0.2}Zn_{0.6}Fe_{2-x}Ho_xO_4$ spinel ferrites catalyst (Scheme 1).

Ethyl 6-methyl-4-(4-pyridyl)-2-oxo-1,2,3,4-tetrahydropyridimidine-5-carboxylate (4 g): ^{1}H NMR (DMSO d_6 , 300 MHz) δ9.38 (s, 1H, NH), 8.50 (d, 2H), 7.85 (s, 1H, NH), 7.20 (d, 2H), 5.15 (d, 1H, *J* = 3.3 Hz, H-4), 4.00 (q, 2H, OCH_2), 2.27 (s, 3H, CH_3), 1.09 (t, 3H, *J* = 7.2 Hz, CH_3); Mass (ES/MS) : *m/z* 260 (M−H, 100%).

Catalytic efficiency $Ni_{0.2}Cu_{0.2}Zn_{0.6}Fe_{2-x}Ho_xO_4$ spinel ferrites studied by screening five compositions x = 0.0, 0.02, 0.04, 0.06 and 0.08 to find out best ferrite composition (catalyst) for 3,4-dihydropyrimidin-2(1H)-one (4a) synthesis as representative reaction. The 3,4-dihydropyrimidin-2(1H)-one compound 4a**,** was obtained with 95% yield with $Ni_{0.2}Cu_{0.2}Zn_{0.6}Fe_{2-x}Ho_xO_4$ (x = 0.06) spinel ferrites catalyst rapidly (100 min) compared to other spinel ferrites compositions(x = 0.0, 0.02, 0.04 and 0.08).

The quantity of ferrite composition (catalyst load) was optimized for model reaction (**4a**). The spinel ferrite as a catalyst was used in varying quantity of 0, 5, 10, 15 and 20 mol %. The decrease in ferrite catalyst quantity from 20 to 10 mol % does not affect the yield (Table 5). Therefore, 10 mol % of the catalyst $Ni_{0.2}Cu_{0.2}Zn_{0.6}Fe_{2-x}Ho_xO_4$(x = 0.6) spinel ferrites was considered to obtain the maximum yield (95%) in less reaction time (10 min).

The generality of this approach was assessed by reacting various aldehydes with 1,3-dicarbonyl compound (2) and urea or thiourea (3) under optimized conditions to obtain substituted 3,4-dihydropyrimidin-2(1H)-ones (4a-h) (Scheme 1) (Table 6).

In heterogeneous catalysis, reusability of the catalyst is an important aspect. The investigation of recovery and reusability of the catalyst was performed for model reaction (**4a**). Catalyst was recycled after the completion of reaction. For this a strong magnet

Table 5
Optimization of reaction conditions and catalyst load (mol %) of $Ni_{0.2}Cu_{0.2}Zn_{0.6}Fe_{2-x}Ho_xO_4$ (x = 0.0 6) nanoparticles for the synthesis of 3,4-dihydropyrimidin-2(1H)-ones (4a).

Entry	Catalyst (nanoparticles)	Catalyst loading (mol %)	Time (min)	Yield of 4a, * %
1	$Ni_{0.2}Cu_{0.2}Zn_{0.6}Fe_{2-x}Ho_xO_4$ (x = 0.0)	20	180	65
2	$Ni_{0.2}Cu_{0.2}Zn_{0.6}Fe_{2-x}Ho_xO_4$ (x = 0. 02)	20	170	81
3	$Ni_{0.2}Cu_{0.2}Zn_{0.6}Fe_{2-x}Ho_xO_4$ (x = 0. 04)	20	150	85
4	$Ni_{0.2}Cu_{0.2}Zn_{0.6}Fe_{2-x}Ho_xO_4$ (x = 0. 06)	20	100	95
5	$Ni_{0.2}Cu_{0.2}Zn_{0.6}Fe_{2-x}Ho_xO_4$ (x = 0. 08)	20	100	79
6	$Ni_{0.2}Cu_{0.2}Zn_{0.6}Fe_{2-x}Ho_xO_4$ (x = 0. 06)	15	100	95
7	$Ni_{0.2}Cu_{0.2}Zn_{0.6}Fe_{2-x}Ho_xO_4$ (x = 0. 06)	10	100	95
8	$Ni_{0.2}Cu_{0.2}Zn_{0.6}Fe_{2-x}Ho_xO_4$ (x = 0. 06)	5	175	77
9	No Catalyst	–	240	30

*Hereinafter, isolated yield of pure product.

Table 6
$Ni_{0.2}Cu_{0.2}Zn_{0.6}Fe_{2-x}Ho_xO_4$ (x = 0. 06) catalyzed synthesis of 3,4-dihydropyrimidin-2(1H)-ones.

Entry	R	R'	x	Time (min)	Yield (%)	M.P. (°C)	
						Observed	Reported [24,38-40]
4a	C_6H_5	C_2H_5O	O	100	95	201–203	200–202
4b	4-$NO_2C_6H_4$	C_2H_5O	O	120	92	208–209	205–207
4c	4-ClC_6H_4	C_2H_5O	O	110	93	213	210–212
4d	4-OHC_6H_4	C_2H_5O	O	130	94	231–232	228
4e	$CH_3CH_2(CH_2)_2$	C_2H_5O	O	120	88	160–161	157–158
4f	3-$NO_2C_6H_4$	C_2H_5O	O	150	90	228–229	225–227
4 g	4-pyridyl	C_2H_5O	O	95	95	186–187	185–186
4 h	C_6H_5	C_2H_5O	S	95	95	209–212	208–210

was used to fix it at the bottom of the flask. The fixed solid catalyst washed twice with acetone. The next run of reaction was preceded by introducing the fresh substrate into the flask. The catalyst was effectively reusable 5 times without losing its catalytic performance. (Cycle number and yield of 4**a**: 1, 95%; 2, 95%; 3, 95%; 4, 94%; 5, 93%).

The work-up process was very simple and first catalyst was removed magnetically then the entire mixture transferred into ice water. The product precipitates out which is separated by filter paper, washed with water and dried. The as-obtained product was purified by recrystallization using ethanol as a solvent. The efficiency, easy handling and mild nature are advantageous aspect of the catalyst.

4. Conclusions

Ho^{3+} substituted Ni-Cu-Zn ferrites with composition $Ni_{0.2}Cu_{0.2}Zn_{0.6}Fe_{2-x}Ho_xO_4$ (x = 0.00 to 0.08 in steps of 0.02) were successfully synthesised by sol–gel auto combustion method. Precursor powders calcinated at 460 °C. The observed elemental analysis from EDAX was in good agreement with the theoretical stoichiometry. The lattice constant, X-ray density and hoping lengths increased with increase in Ho^{3+}. The D_{XRD} was decreased from 26.2 to 19.9 nm with the substitution of Ho^{3+}. The low frequency IR band ν_2 in the range 409–438 cm^{-1} is assigned octahedral site and high frequency IR band ν_1 in the range 565–568 cm^{-1} assigned tetrahedral site. SEM images confirmed the porous nature with a fine-grained microstructure. TEM images revealed sphere-like nanostructures and particles with agglomeration to some extent due to their magnetic interactions. Saturation magnetization decreased while observed magneton number increased with the increase in Ho^{3+}concentration. 3,4-dihydropyrimidin-2(1H)-ones synthesized using the one-pot three-component condensation of aromatic aldehydes, 1,3 dicarbonyl compounds and urea using magnetic Ho^{3+} doped Ni-Cu-Zn spinel ferrites catalyst.

CRediT authorship contribution statement

U.M. Mandle: Investigation, Writing - original draft. **R.M. Tigote:** Formal analysis, Writing - review & editing. **K.S. Lohar:** Conceptualization, Supervision, Writing - review & editing. **B.L. Shinde:** Investigation, Methodology, Formal analysis, Writing - original draft.

Declaration of Competing Interest

The authors declare that they have no known competing financial interests or personal relationships that could have appeared to influence the work reported in this paper.

References

[1] T. Krishnaveni, B.R. Kanth, V.S.R. Raju, S.R. Murthy, J. Alloys Compd. 414 (2006) 282–286.
[2] C.B. Carter, M.G. Norton, Ceramic materials: science and engineering, New York: Springer. 716 (2007) 712.
[3] S. Singhal, S.K. Barthwal, K. Chandra, J. Magn. Magn. Mater. 296 (2006) 94–103.
[4] B.L. Shinde, L.A. Dhale, V.S. Suryavanshi, K.S. Lohar, Acta Chim. Slov. 64 (2017) 931–937.
[5] Z. Shi, Y. Zeng, X. Chen, F. Zhou, L. Zheng, G. Wang, R. Yu, J. Magn. Magn. Mater. 498 (2020) 166222.
[6] R. Sharma, P. Thakur, P. Sharma, V. Sharma, J. Alloys Compd. 704 (2017) 7–17.
[7] M. Sadeghinia, J.S. Shayeh, F. Fatemi, M. Rahmandoust, A. Ehsani, M. Rezaei, Int. J. Hydrog. Energy. 44 (2019) 28088–28095.
[8] A. Yakubu, A. Zulkifly, S. Sahabi, Global Journal of Material Science and Engineering 1 (2019) 1–4.
[9] P.D. Prasad, J. Hemalatha, J. Magn. Magn. Mater. 484 (2019) 225–233.
[10] B.L. Shinde, L.A. Dhale, U.M. Mandle, K.S. Lohar, Int. Res. J. Pharm. 10 (2019) 50–55.
[11] Y. Zheng, L. Jia, F. Xu, G. Wang, X. Shi, H. Zhang, Ceram. Int. 45 (2019) 22163–22168.
[12] S.M. Kabbur, S.D. Waghmare, D.Y. Nadargi, et al., J. Magn. Magn. Mater. 473 (2019) 99–108.
[13] S. Karimunnesa, A.A. Ullah, M.R. Hasan, et al., J. Magn. Magn. Mater. 457 (2018) 57–63.
[14] J. Zhu, H. Bienaymé, Multicomponent Reactions, Wiley-VCH, Weinheim, 2005.
[15] R.V. Orru, M. de Greef, Synthesis 2003 (2003) 1471–1499.
[16] F. Nemati, M.G. Afkham, A. Elhampour, Green Chem. Lett. Rev. 7 (1) (2014) 79–84.
[17] C.S. Narasimhan, C.S. Swamy, Applied Catalysis 2 (1982) 315–328.
[18] A. Maleki, Tetrahedron Lett. 54 (2013) 2055–2059.
[19] M.Z. Kassaee, H. Masrouri, F. Movahedi, Appl. Catal. A 395 (2011) 28–33.
[20] M. Esmaeilpour, A.R. Sardarian, J. Javidi, Appl. Catal. A 445 (2012) 359–367.
[21] P. Biginelli, Gazz. Chim. Ital 23 (1893) 360–416.
[22] J. Safari, S. Gandomi-Ravandi, New J. Chem. 38 (2014) 3514–3521.
[23] J. Peng, Y. Deng, Tetrahedron Lett. 4 (2001) 5917–5919.
[24] Y. Ma, C. Qian, L. Wang, M. Yang, The Journal of organic chemistry 65 (2000) 3864–3868.
[25] W. Su, J. Li, Z. Zheng, Y. Shen, Tetrahedron Lett. 46 (2005) 6037–6040.
[26] E. Kolvari, N. Koukabi, O. Armandpour, Tetrahedron 70 (2014) 1383–1386.
[27] J.T. Starcevich, T.J. Laughlin, R.S. Mohan, Tetrahedron Lett. 54 (2013) 983–985.
[28] B.J. Ahn, M.S. Gang, K. Chae, Y. Oh, J. Shin, W. Chang, J. Ind. Eng. Chem. 14 (2008) 401–405.
[29] M.N. Akhtar, M.A. Khan, et al., Ceram. Int. 40 (2014) 15821–15829.
[30] E. Pervaiz, I.H. Gul, J. Magn. Magn. Mater. 349 (2014) 27–34.
[31] B.D. Cullity, Elements of X-ray diffraction, (Addison-Wesley Publ. Comp. Inc., Reading, Massachusetts, U.S.A, 1956, p. 99.
[32] L. Kumar, M. Kar, J. Exp. Nanosci. 9 (2014) 362–374.
[33] S.E. Shirsath, R.H. Kadam, et al., J. Alloys Compd. 575 (2013) 145–151.
[34] R.D. Waldron, Phys. Rev. 99 (1955) 1727.
[35] E.W. Gorter, Philips Research Reports 9 (1954) 321–365.
[36] P.A. Shaikh, R.C. Kambale, A.V. Rao, Y.D. Kolekar, J. Magn. Magn. Mater. 322 (2010) 718–726.
[37] L. Neel, Ann. Phys 3 (1948) 137–198.
[38] C.V. Reddy, M. Mahesh, et al., Tetrahedron Lett. 43 (2002) 2657–2659.
[39] Q. Sun, Y.Q. Wang, Z.M. Ge, T.M. Cheng, R.T. Li, Synthesis 2004 (2004) 1047–1051.
[40] N.Y. Fu, Y.F. Yuan, Z. Cao, S.W. Wang, J.T. Wang, C. Peppe, Tetrahedron 58 (2002) 4801–4807.